



# Superplastic martensitic Mn–Si–Cr–C steel with 900% elongation

H. Zhang<sup>a,b,\*</sup>, B. Bai<sup>b</sup>, D. Raabe<sup>a,\*</sup>

<sup>a</sup> Max-Planck Institut für Eisenforschung, Max-Planck Str 1, 40237 Düsseldorf, Germany

<sup>b</sup> Key Laboratory for Advanced Materials, Department of Materials Science and Engineering, Tsinghua University, 100084 Beijing, People's Republic of China

Received 17 April 2011; received in revised form 25 May 2011; accepted 26 May 2011  
Available online 23 June 2011

## Abstract

High-strength (1.2–1.5)C–(2–2.5)Mn–(1.5–2)Si–(0.8–1.5)Cr steels (mass%) consisting of martensite and carbides exhibit excellent superplastic properties (e.g. strain rate sensitivity  $m \approx 0.5$ , elongation  $\approx 900\%$  at 1023 K). A homogeneous martensitic starting microstructure is obtained through thermomechanical processing (austenitization plus 1.2 true strain, followed by quenching). Superplastic forming leads to a duplex structure consisting of ferrite and spherical micro-carbides. Through 1.5–2% Si alloying, carbides precipitate at hetero-phase interfaces and martensite blocks at the beginning of superplastic forming. Via Ostwald ripening, these interface carbides grow at the expense of carbides precipitating at martensite laths, thereby promoting ferrite dynamic recrystallization. Simultaneously, carbides at ferrite grain boundaries retard the growth of recrystallized ferrite grains. Due to 2–2.5% Mn and 0.8–1.5% Cr alloying, carbide coarsening is suppressed owing to the slow diffusion of these elements. As a result, fine and homogeneous ferrite plus spherical carbide duplex microstructures with a ferrite grain size of  $\sim 1.5 \mu\text{m}$  are obtained after superplastic forming.

© 2011 Acta Materialia Inc. Published by Elsevier Ltd. All rights reserved.

**Keywords:** Steel; Superplasticity; Martensite; Carbide; Thermomechanical processing

## 1. Introduction

Superplasticity of steels is of interest, from both engineering and microstructural perspectives. On the engineering side, superplasticity of steels with several 100% elongation allows the manufacturing of parts with nearly arbitrarily complex shapes. On the structure–property side, the richness of transformation phenomena in the Fe–C system can be used for tailoring microstructures and optimal strength–ductility profiles after superplastic forming. The art of designing superplastic steels hence consists of two steps: first, the starting microstructure has to be optimized to render the steel superplastic when formed in a suited

temperature–strain rate corridor ( $\sim 1000 \text{ K}$ ,  $\sim 10^{-4}$ – $10^{-3} \text{ s}^{-1}$ ); and second, the deformed material should assume a homogeneous and sufficiently fine microstructure after superplastic forming (grain size in the micrometer range) to provide excellent mechanical properties in the final product. The current paper reports about such an attempt.

Various studies have discussed methods for obtaining microstructures via thermomechanical processing that are advantageous for superplastic forming of steels, including temperature cycling across the ferrite–austenite transformation [1,2], hot and warm deformation combined with divorced eutectoid transformation [3,4], multiple-pass heat treatment [5], severe plastic deformation [6–8], cold rolling with subsequent annealing [9–12] and warm deformation of martensite [13,14]. The effect of alloying (e.g. Si, Al, Cr) in conjunction with thermomechanical processing on the superplasticity of steels has also been discussed [15–17]. It was observed that thermomechanical processing can be simplified through (2–2.5)Mn–(1.5–2)Si–(0.8–1.5)Cr

\* Corresponding authors: Department of Materials Science and Engineering, Tsinghua University, Beijing, 100084, PR China. Tel.: +86 10 62772976, Max-Planck Institut für Eisenforschung, Max-Planck Str 1, 40237 Düsseldorf, Germany. Tel.: +49 0211 6792 340.

E-mail addresses: [zhanghan06@mails.tsinghua.edu.cn](mailto:zhanghan06@mails.tsinghua.edu.cn) (H. Zhang), [d.raabe@mpie.de](mailto:d.raabe@mpie.de) (D. Raabe).

alloying (mass%). For example, the superplasticity of medium carbon steels was realized via complicated temperature cycling across the ferrite–austenite transformation [2]. Through Mn–Si–Cr alloying, even without application of temperature cycling, medium carbon steels were also found to exhibit superplastic characteristics during warm deformation of an initially martensitic starting microstructure [13]. For optimal superplasticity, it is required to optimize the thermomechanical processing to obtain finer starting microstructures via adequate deformation and heat treatment. Thermomechanical deformation (true strain of 1.2) applied above the austenite–pearlite equilibrium transformation temperature (i.e.  $A_1$  temperature) was identified as beneficial for obtaining fine martensite (martensite block size  $<10\ \mu\text{m}$ ) in Mn–Si–Cr alloyed medium carbon steels [13,14]. Controlling austenitization and the subsequent cooling rate led to the formation of a fine microstructure (martensite plus spherical carbides with a martensite block size  $<10\ \mu\text{m}$ ) in Mn–Si–Cr alloyed ultrahigh carbon steels [18]. Such microstructures were observed to reveal superplastic flow. The aim of these improvement schemes for the preceding thermomechanical processing is to obtain finer microstructures prior to superplastic forming (e.g. refined martensite), thereby providing more carbide precipitation sites and, hence, improving the dispersion of carbides during superplastic forming. It was observed that the dispersed carbides gradually coarsen and promote the formation of microstructures that are beneficial for superplasticity (e.g. a fine and homogeneous duplex ferrite plus spherical carbide microstructure with a ferrite grain size  $\sim 1.5\ \mu\text{m}$ ) during superplastic forming. Such microstructures are desired because submicron-sized carbides at ferrite grain boundaries can promote ferrite dynamic recrystallization (DRX) and retard the growth of ferrite grains in the superplastic regime [13,18].

Although some results about superplasticity of Mn–Si–Cr alloyed steels were reported in Refs. [13,14,18], there is insufficient understanding of the effects of the initial thermomechanical processes on superplasticity, the superplastic mechanisms and the final microstructure–property relations of these steels after forming. Qualitatively, it was observed that Mn–Si–Cr alloying in conjunction with thermomechanical processing determines the starting microstructures and the structure evolution during superplastic forming and, hence, also the final mechanical properties of the superplastically formed samples [13,15]. Therefore, the superplastic behavior is studied here in more detail from two aspects: first, the specific effect of Mn–Si–Cr alloying and, second, the thermomechanical processing that precedes superplastic forming. In this study, a 0.46C–2.18Mn–1.46Si–1.05Cr steel (denoted by 0.5CMnSiCr; compositions in mass%) and a 0.48C–0.68Mn–0.25Si–0.15Cr steel (denoted by 0.5C) were used to analyze the effect of Mn–Si–Cr alloying on superplasticity. A 1.31C–2.17Mn–1.83Si–1.02Cr steel (denoted by 1.3CMnSiCr) was used to analyze the effect of the initial thermomechanical processing. Different types of thermomechanical

processes were applied in this study, including the above-mentioned deformation scheme (true strain of 1.2 at 1073 K) in order to obtain refined initial microstructures prior to superplastic forming. The cooling condition after deformation was used as a variable in order to explore different resulting microstructures. Previous studies [14,18] showed that selecting a suitable superplastic forming temperature after thermomechanical processing may finally lead to ultrahigh strength of the steel after superplastic forming even without any supplementary heat treatment. Therefore, the superplastic forming temperature was also varied.

As a characteristic parameter connected with superplasticity [19], the strain rate sensitivity ( $m$ ) was used for the evaluation of superplasticity. Generally, a value of  $m \geq 0.3$  is considered characteristic of superplasticity. Typically, superplastic elongation of metals increases with the  $m$ -value [20]. Therefore, the aim of the study was the thermomechanical design of steel microstructures with high strain rate sensitivity as a necessary, but not sufficient, precondition for superplastic flow. However, for ultrahigh strength steels (e.g. the ultrahigh carbon 1.3CMnSiCr steel used in this study), brittle phases such as martensite and carbides may cause internal stress concentrations or even cavities during deformation. Such effects limit superplastic elongation even at high  $m$ -values. Therefore, the  $m$ -value alone is not sufficient to evaluate the superplastic behavior. In this study, the elongation and the strain rate sensitivity were therefore both used to quantify and compare the superplastic behavior of 0.5CMnSiCr and 1.3CMnSiCr alloys.

## 2. Experimental methods

### 2.1. Small specimen experiments

Small specimen thermomechanical processing (before superplastic forming) was conducted on cylinders 8 mm in diameter and 90 mm long cut from forged billets of alloys 0.5CMnSiCr and 0.5C (Fig. 1a and b). Pre-deformation (true strain 1.2) was applied above  $A_{e3}$  ( $A_{e3}$ , temperature above which no ferrite exists in equilibrium) followed by air cooling or water quenching, respectively. After processing, cylinders 6 mm in diameter and 10 mm long (i.e. specimens 1–3 according to the processing outlined in Fig. 1) were cut from the central region for subsequent evaluation of the superplastic behavior during warm deformation (warm deformation hereafter generally refers to small specimen superplastic testing). The deformation conditions during superplastic deformation at 973 K are shown in Table 1. All superplastic forming cycles discussed in this paper consist of three sequential strain regimes, namely, the first strain regime ( $R_1$ ), the transition regime ( $R_t$ ) and the second strain regime ( $R_2$ ). The regimes  $R_1$  ( $R_2$ ) with a total true strain of 0.2 consist of five sequential strain steps, i.e.  $R_{11}$ ,  $R_{12}$ ,  $R_{13}$ ,  $R_{14}$ , and  $R_{15}$  (similarly,  $R_{21}$ ,  $R_{22}$ ,  $R_{23}$ ,  $R_{24}$  and  $R_{25}$ ). Each of these sub-regimes imposed a true strain step of 0.04 at a specific strain rate, see Table 1

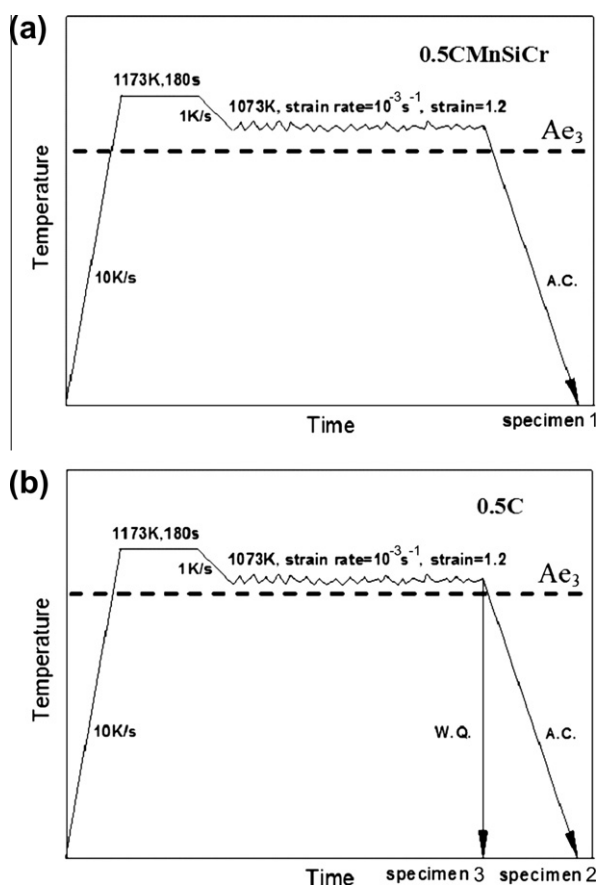


Fig. 1. Schematic diagram explaining the small specimen thermomechanical processing before superplastic forming of alloys (a) 0.5CMnSiCr and (b) 0.5C; air cooling, AC; water quenching, WQ; specimens 1–3 obtained from this initial processing served as input materials to the subsequent superplastic forming experiments; Ae3, temperature above which no ferrite exists in equilibrium.

(e.g. R<sub>11</sub> indicates a true strain step of 0.04 at 10<sup>-4</sup> s<sup>-1</sup> within the strain regime R<sub>1</sub>). A true strain of 0.3 at 10<sup>-3</sup> s<sup>-1</sup> was applied within R<sub>1</sub> in order to focus on the difference in strain rate sensitivity between deformation regimes R<sub>1</sub> and R<sub>2</sub>. The strain rate change method was employed to measure the strain rate sensitivity within R<sub>1</sub> and R<sub>2</sub>. In order to study the microstructure evolution during superplastic forming, water quenching was used immediately after warm deformation. The small specimen experiments were performed by uniaxial compression testing on a Gleeble 1500D instrument.

Table 1  
Deformation conditions during superplastic warm deformation at 973 K.

Strain regime	First strain regime (R <sub>1</sub> )					Transition regime (R <sub>t</sub> )	Second strain regime (R <sub>2</sub> )				
	R <sub>11</sub>	R <sub>12</sub>	R <sub>13</sub>	R <sub>14</sub>	R <sub>15</sub>		R <sub>21</sub>	R <sub>22</sub>	R <sub>23</sub>	R <sub>24</sub>	R <sub>25</sub>
Strain	0.04	0.04	0.04	0.04	0.04	0.3	0.04	0.04	0.04	0.04	0.04
Strain rate, s <sup>-1</sup>	10 <sup>-4</sup>	2 × 10 <sup>-4</sup>	4 × 10 <sup>-4</sup>	10 <sup>-3</sup>	3 × 10 <sup>-3</sup>	10 <sup>-3</sup>	10 <sup>-4</sup>	2 × 10 <sup>-4</sup>	4 × 10 <sup>-4</sup>	10 <sup>-3</sup>	3 × 10 <sup>-3</sup>

The superplastic forming cycles consist of three sequential strain regimes, namely, the first strain regime (R<sub>1</sub>), the transition regime (R<sub>t</sub>), and the second strain regime (R<sub>2</sub>). Regimes R<sub>1</sub> (R<sub>2</sub>) with a total true strain of 0.2 consist of five sequential strain steps, i.e. R<sub>11</sub>, R<sub>12</sub>, R<sub>13</sub>, R<sub>14</sub>, and R<sub>15</sub> (similarly, R<sub>21</sub>, R<sub>22</sub>, R<sub>23</sub>, R<sub>24</sub> and R<sub>25</sub>). Each of these sub-regimes imposed a true strain step of 0.04 at a specific strain rate (e.g. R<sub>11</sub> indicates a strain step of 0.04 at 10<sup>-4</sup> s<sup>-1</sup> within regime R<sub>1</sub>).

## 2.2. Large-scale thermomechanical treatment

Large-scale thermomechanical processing was applied to alloys 0.5CMnSiCr and 1.3CMnSiCr in order to obtain tensile samples for the evaluation of their superplastic properties. Compared with the small specimens, the large-scale treatment was conducted to obtain sufficiently large and homogeneous samples for superplastic characterization. Rectangular forged billets 100 × 60 × 60 mm<sup>3</sup> (length × width × thickness) were cut to conduct continuous rolling after holding at 1223 K for 1 h. The continuous rolling used three passes (reduction ~10 mm each pass), leading to a final plate thickness of 30 mm. The final rolling temperature was ~1073 K. Air cooling and water quenching were used after rolling to obtain air-cooled (AC) and water-quenched (WQ) tensile samples from the center of the rolled plates, respectively.

## 2.3. Tensile testing for evaluation of superplastic properties

A high-temperature tensile testing machine (Instron Model 1185) was used to quantify superplastic elongation. Bone-shaped flat tensile samples (gauge length 10 mm) were machined (Fig. 2). During testing, the crosshead displacement speed was set to 0.5 mm min<sup>-1</sup> to keep the initial strain rate at ~10<sup>-4</sup> s<sup>-1</sup>. The limited gauge area of uniform temperature may lead to non-uniformity during testing when large samples are used. Therefore, tensile samples with a short gauge length of 5 mm were employed for the tensile testing of the 1.3CMnSiCr samples, which revealed very high elongation values up to 900%.

## 2.4. Microscopy

Microstructural observation (secondary electron imaging), composition analysis (energy-dispersive X-ray spectroscopy, EDX), and texture measurements (electron backscatter diffraction) were conducted using scanning electron microscopy (SEM; JEOL JSM-6301F). The volume fractions of martensite, pearlite and ferrite were estimated using Imageproplus analysis software produced by Media Cybernetics Company [21]. The linear intercept method [22] was used to measure the size of the ferrite grains and spherical carbides.

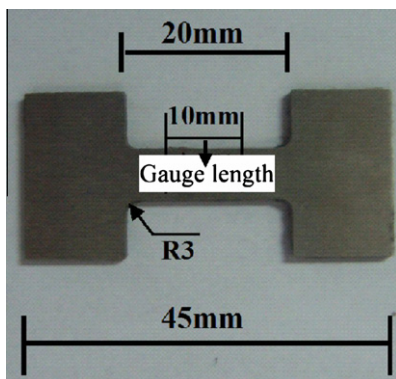


Fig. 2. Tensile sample shapes used for high-temperature tensile testing (973 K) in the superplastic regime for small and average elongations (several 100%). Note that specimens tested at even higher temperatures of 1023 K (with elongations up to 900%) used a smaller central gauge portion in order to ensure temperature homogeneity.

### 3. Results

#### 3.1. Microstructure

Fig. 3 shows the secondary electron imaging results for specimens 1–3 (specimen 1, alloy 0.5CMnSiCr; specimens 2 and 3, alloy 0.5C as obtained by thermomechanical processing; Fig. 1). Fig. 3a and c shows the microstructures of specimens 2 and 3 (alloy 0.5C) obtained after pre-processing (before superplastic forming) (Fig. 1b). For the 0.5C alloy, the microstructure of specimen 2 contains pearlite (P,  $\sim 75$  vol.%), martensite (M,  $\sim 20$  vol.%), and ferrite (F,  $\sim 5$  vol.%), which is different from that of specimen 3 containing martensite ( $\sim 93$  vol.%), pearlite (as shown within the dashed circle,  $\sim 5$  vol.%) and ferrite (as shown within the solid circle  $\sim 2$  vol.%). For alloy 0.5CMnSiCr, the microstructure of specimen 1 obtained after the processing described in Fig. 1a contains 100 vol.% martensite (Fig. 3e).

The microstructures of specimens 1–3 after superplastic deformation at 973 K (and subsequent quenching) are shown in Fig. 3f, b and d. Corresponding high-resolution SEM images are given in Fig. 3g for specimen 3 after superplastic deformation at 973 K (same state as in Fig. 3d) and in Fig. 3h for specimen 1 after superplastic deformation at 973 K (same state as in Fig. 3f).

It can be seen that the duplex microstructure (ferrite plus spherical carbides) in Fig. 3f and h is very homogeneous. The upper-right micrograph of the area marked by the red<sup>1</sup> dashed rectangle clearly shows that micron-sized ferrite grains are surrounded by submicron-sized carbides. The average size of the ferrite grains and of the submicron-sized carbides located at ferrite grain boundaries are  $\sim 1.5$   $\mu\text{m}$  and  $0.5$   $\mu\text{m}$  in diameter, respectively. Compared with the microstructure obtained after superplastic forming (Fig. 3f), the microstructures visible

in Fig. 3b, d and g are more inhomogeneous and coarse (ferrite grain size  $\sim 5$   $\mu\text{m}$ ). In Fig. 3b, carbide spheroidization occurs within the initial pearlite zone (solid circle). DRX of ferrite has taken place within the area marked by the solid rectangle. Fig. 3d and g shows that DRX of the ferrite was even more complete than in Fig. 3b, and the average size of the ferrite grains formed during DRX ( $\sim 5$   $\mu\text{m}$ , green arrows) is larger than that in Fig. 3f and h ( $\sim 1.5$   $\mu\text{m}$ ).

Further, it is observed that more nanometer-sized carbides are dispersed in the microstructure shown in Fig. 3d and g (number fraction  $\sim 70\%$ ) than revealed in Fig. 3f and h (number fraction  $\sim 15\%$ ). The number fraction describes in this case the number of the nanometer-sized carbides divided by the total number of all carbides, including nanometer-sized and submicron-sized carbides. Also, it is observed that the average size of the submicron-sized carbides determined for Fig. 3d and g ( $\sim 0.8$   $\mu\text{m}$  in diameter) is larger than that observed in Fig. 3f and h ( $\sim 0.5$   $\mu\text{m}$  in diameter). The diameter distribution amounts to  $\sim 0.8 \pm 0.3$   $\mu\text{m}$  for Fig. 3d and g and  $\sim 0.5 \pm 0.2$   $\mu\text{m}$  for Fig. 3f and h.

Fig. 4a and b shows the AC and WQ microstructures obtained from the center of the rolled plates for alloy 1.3CMnSiCr after the large-scale thermomechanical treatment (1 h holding at 1223 K plus 50% reduction at 1223–1073 K followed by cooling), respectively. The AC microstructure contains mainly spherical carbides and lamellar pearlite, while the WQ microstructure reveals mainly spherical carbides and martensite. Fig. 4c and d shows the AC and WQ microstructures obtained from the center of the rolled plates for alloy 0.5CMnSiCr after large-scale thermomechanical treatment (1 h holding at 1223 K plus 50% reduction at 1223–1073 K followed by cooling), respectively. The AC and WQ microstructures are composed mostly of martensite.

#### 3.2. EDX

Fig. 5 shows the EDX results of the carbide and ferrite zones in specimen 1 (alloy 0.5CMnSiCr) after superplastic forming at 973 K (i.e. the yellow and blue dots in Fig. 3f), respectively. Attention should be paid to the distribution of Mn, Si and Cr within the red frames. It can be seen that Mn and Cr aggregate at the carbides, while Si partitions mainly into the ferrite.

#### 3.3. Crystallographic texture

The ferrite orientation distribution maps of specimen 1 (alloy 0.5CMnSiCr) and specimen 3 (alloy 0.5C) after superplastic deformation at 973 K are shown in Fig. 6a and d, respectively. Fig. 6b and e reveals the spatial distribution of specific fiber texture components of the microstructures shown in Fig. 6a and d. The yellow and red zones represent the  $\langle 111 \rangle$ ||ND and  $\langle 100 \rangle$ ||ND fiber textures including  $15^\circ$  orientation scatter around the main

<sup>1</sup> For interpretation of color in Figs. 3, 6, 7 and 11, the reader is referred to the web version of this article.

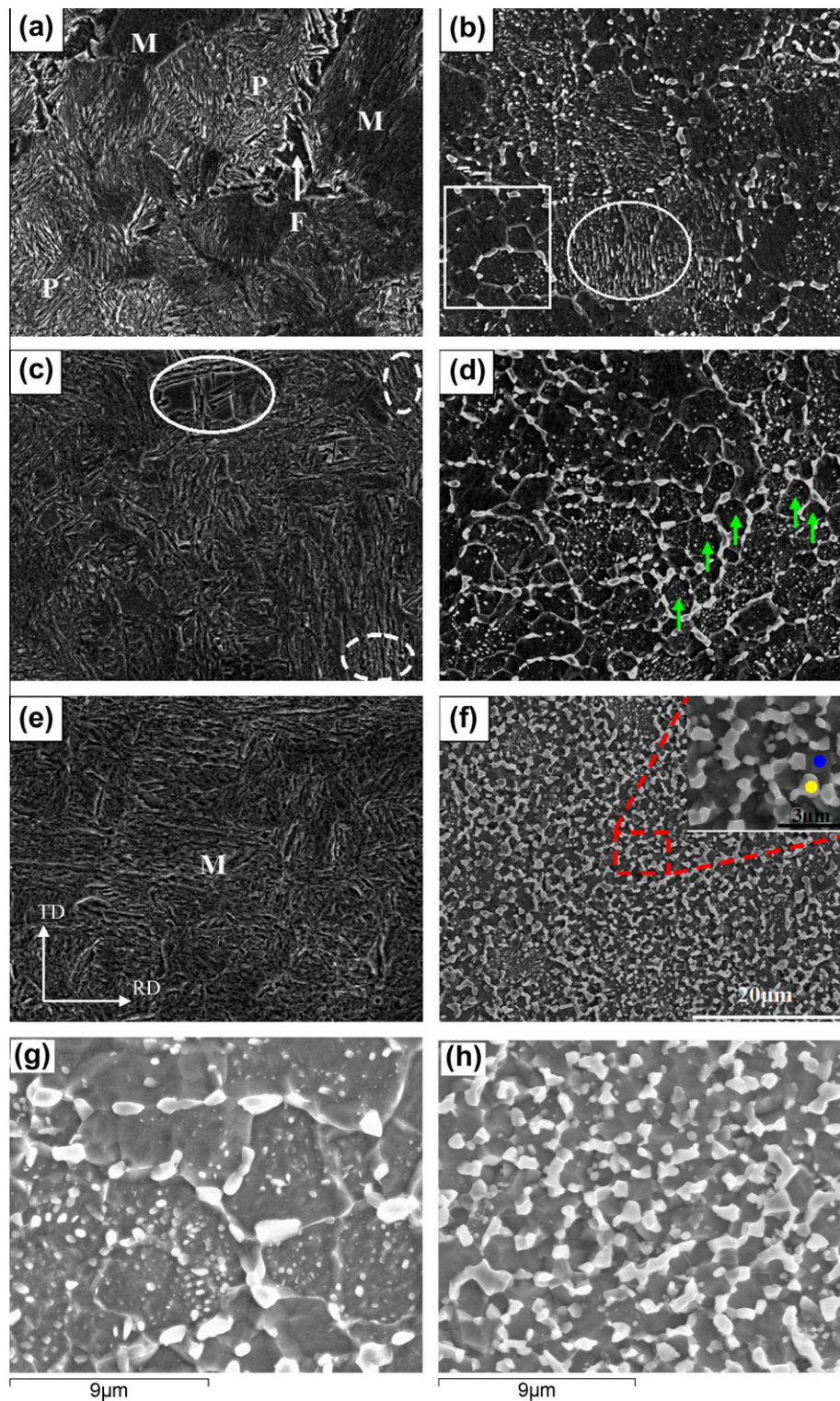


Fig. 3. SEM micrographs: left-hand side, microstructure after initial pre-processing before superplastic testing; right-hand side, microstructure after superplastic warm deformation at 973 K and subsequent quenching. (a) Specimen 2 after initial pre-processing before superplastic testing (alloy 0.5C; M, martensite; P, pearlite; F, ferrite); (b) specimen 2 after superplastic warm deformation at 973 K and subsequent quenching (carbide spheroidization occurs within the solid circle; DRX of ferrite occurs within the solid rectangle); (c) specimen 3 after initial pre-processing before superplastic testing (alloy 0.5C) (within the dashed circle, pearlite; within the solid circle, ferrite); (d) specimen 3 after superplastic warm deformation at 973 K and subsequent quenching (the green arrows denote the ferrite grains formed by DRX); (e) specimen 1 after initial pre-processing before superplastic testing (alloy 0.5CMnSiCr; M, martensite); (f) specimen 1 after warm deformation at 973 K and subsequent quenching (within the red dashed rectangle: (ferrite plus spherical carbides) duplex microstructure; the ferrite and spherical carbide denoted by the blue and yellow dots, respectively); (g) specimen 3 after superplastic warm deformation at 973 K and subsequent quenching as high-resolution SEM micrograph (same state as (d)); (h) specimen 1 after superplastic warm deformation at 973 K and subsequent quenching as high-resolution SEM micrograph (same state as (f)).

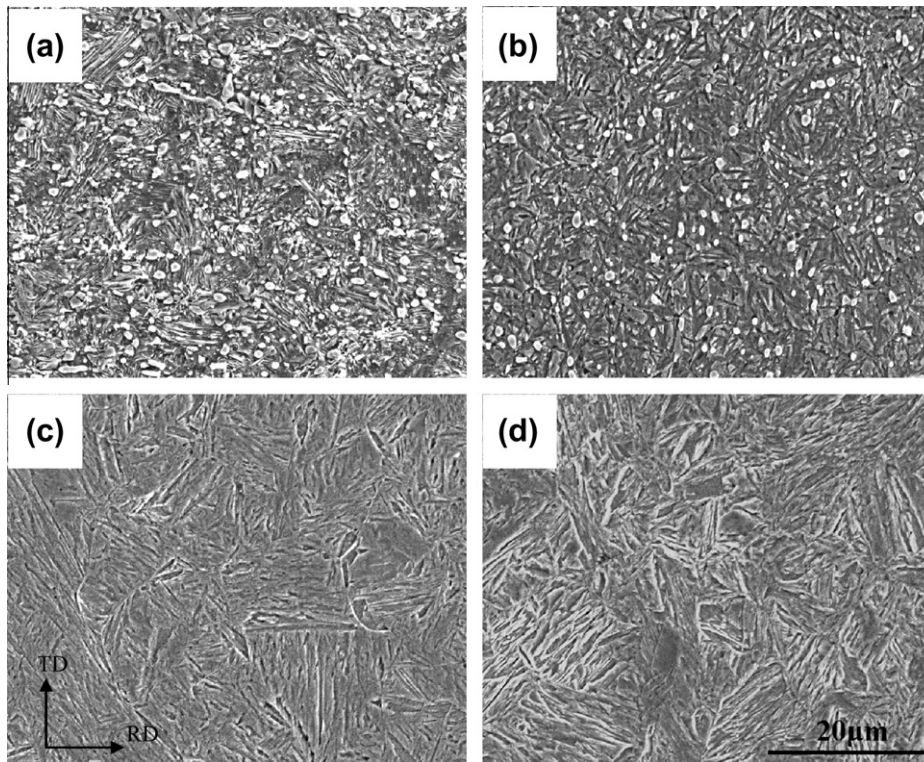


Fig. 4. (a) AC and (b) WQ microstructures obtained from the center of the rolled plates (30 mm) for alloy 1.3CMnSiCr after large-scale thermomechanical treatment; (c) AC and (d) WQ microstructures obtained from the center of the rolled plates (30 mm) for alloy 0.5CMnSiCr after large-scale thermomechanical treatment.

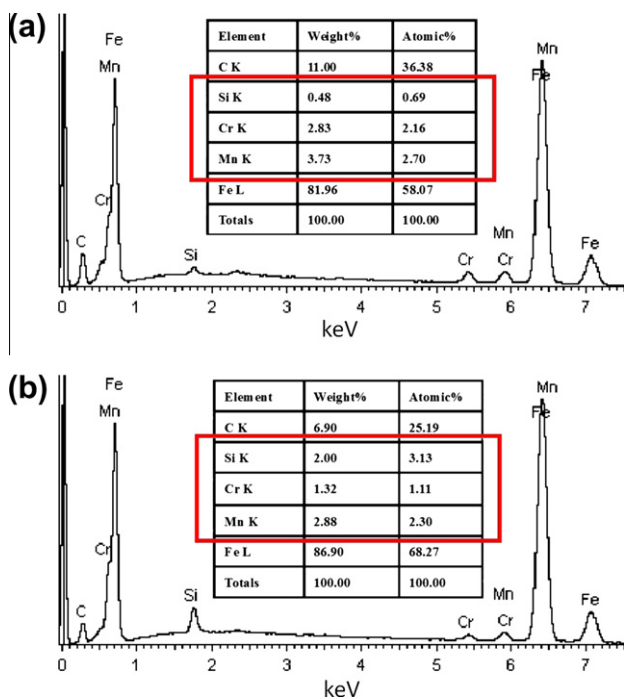


Fig. 5. EDX results of (a) carbides and (b) ferrite in specimen 1 (alloy 0.5CMnSiCr) after warm deformation at 973 K.

crystallographic fiber. Fig. 6g and h shows the pole figures for specimen 1 (alloy 0.5CMnSiCr) and specimen 3 (alloy

0.5C) after superplastic deformation at 973 K. Fig. 6i shows the corresponding orientation distribution functions (ODF).

The data reveal that pronounced orientation distributions are formed. The  $\langle 111 \rangle \parallel \text{ND}$  fiber represent a typical texture formed during DRX of ferrite, while the  $\langle 100 \rangle \parallel \text{ND}$  texture fiber indicates the occurrence of ferrite recovery in steels [9,23–25].

The fraction of the  $\langle 100 \rangle \parallel \text{ND}$  texture fiber component in Fig. 6e (46 area%; alloy 0.5C) is higher than in Fig. 6b (30 area%; alloy 0.5CMnSiCr). This observation suggests that the progress of ferrite recovery during superplastic deformation of specimen 3 (alloy 0.5C) is more intense than that during superplastic forming of specimen 1 (alloy 0.5CMnSiCr). This is also confirmed by Fig. 6i, where the ODF sections reveal for alloy 0.5C a strong prevalence of a texture component close to  $\{001\} \langle 110 \rangle$ , which is indicative of recovery in body-centered cubic (bcc) steels [9,23–26].

In contrast, the fraction of the  $\langle 111 \rangle \parallel \text{ND}$  fiber texture formed during superplastic deformation of specimen 1 (25 area% in Fig. 6b, alloy 0.5CMnSiCr) is higher than that obtained during superplastic deformation of specimen 3 (20 area% in Fig. 6e, alloy 0.5C). This is also confirmed by the ODF analysis shown in Fig. 6i. These data suggests that the DRX or even post-DRX of ferrite in specimen 1 (alloy 0.5CMnSiCr) proceeds more completely than that in specimen 3 (alloy 0.5C) during superplastic forming.

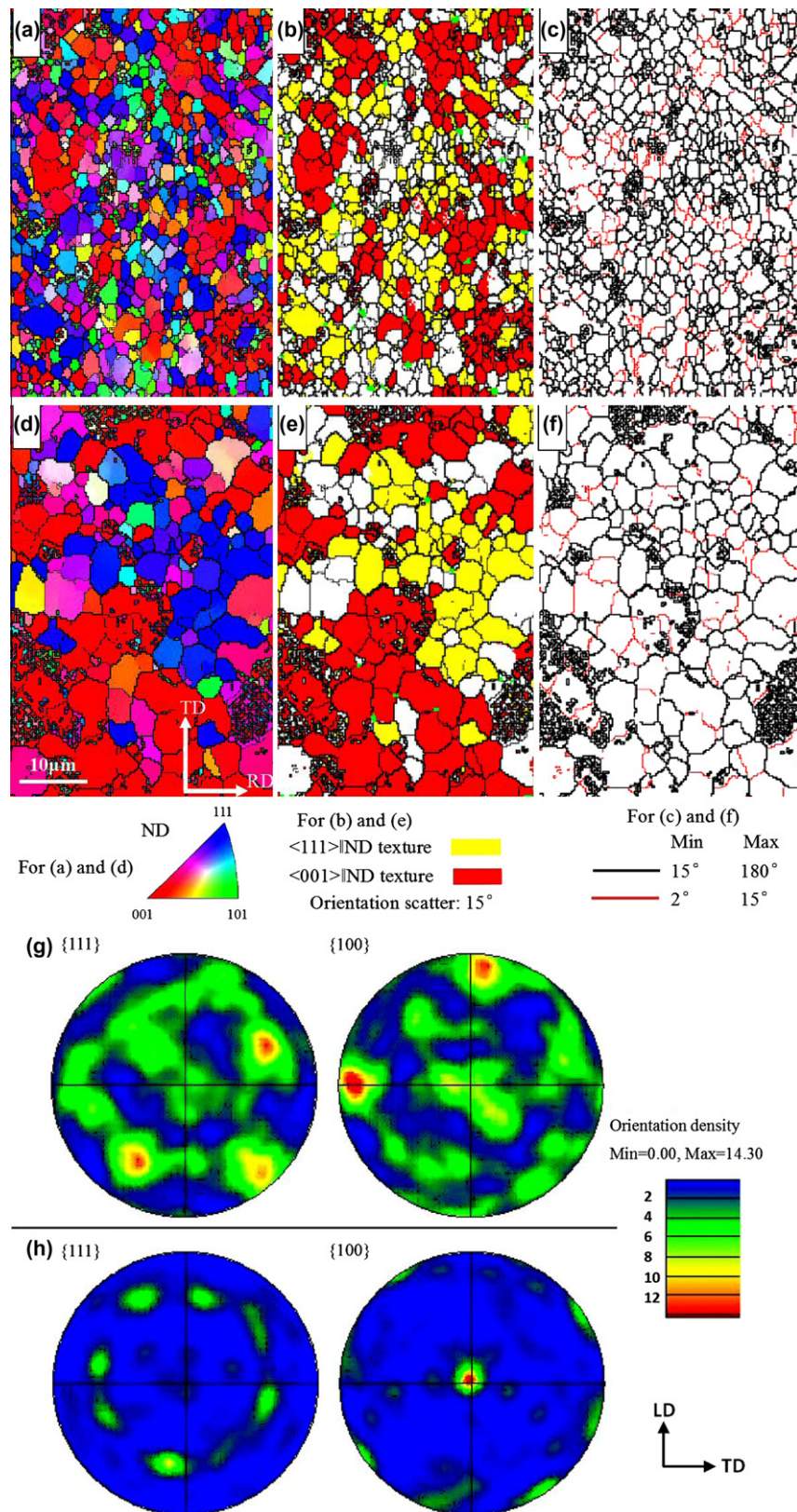


Fig. 6. Alloy 0.5CMnSiCr (specimen 1) after superplastic deformation at 973 K: (a) ferrite orientation distribution map; (b) in-plane distribution of main texture fibers; (c) grain boundary map; (g) pole figures, alloy 0.5C (specimen 3) after superplastic deformation at 973 K: (d) ferrite orientation distribution map; (e) in-plane distribution of main texture fibers; (f) grain boundary map; (h) pole figures (LD, longitudinal direction of flat compressed sample; TD, transverse direction of flat compressed sample; black pixels in (b) and (e), unidentified zones). (i) 2D sections and 3D presentation of the orientation distribution functions of alloy 0.5CMnSiCr (specimen 1) after superplastic deformation at 973 K (top row) and of alloy 0.5C (specimen 3) after superplastic deformation at 973 K (bottom row).

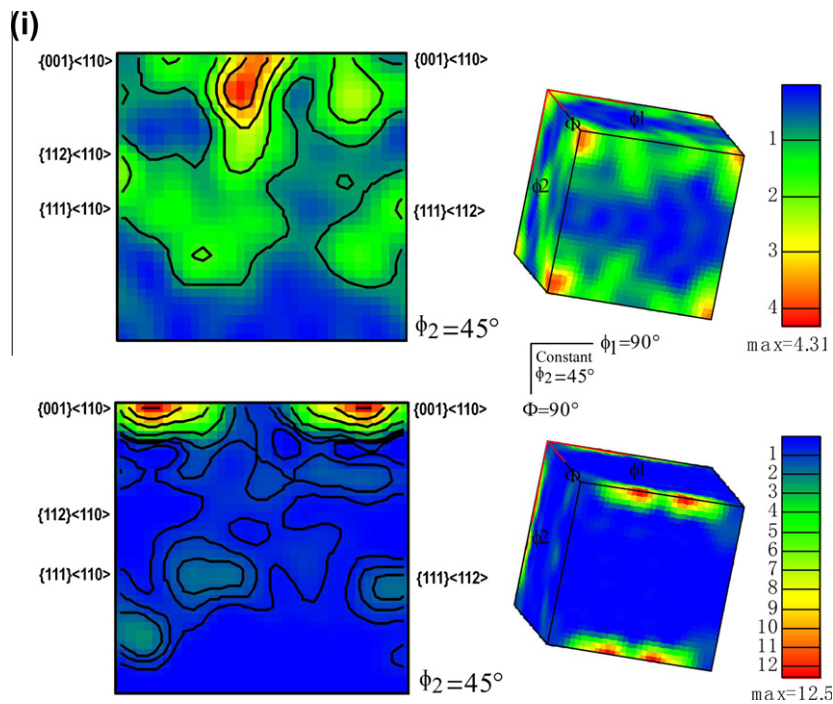


Fig 6. (continued)

The grain boundaries formed in the superplastic regime in specimens 1 and 3 are shown in the grain boundary maps in Fig. 6c and f. The black and red lines denote high-angle ( $\theta > 15^\circ$ ) and low-angle ( $2^\circ < \theta < 15^\circ$ ) grain boundaries, respectively. The density of low-angle grain boundaries in specimen 1 (alloy 0.5CMnSiCr) is larger than in specimen 3 (alloy 0.5C) after superplastic deformation. In addition, some unidentified orientation zones exist (i.e. black areas in Fig. 6b and e), which are the result of dispersed carbides.

Generally, it is admissible that the crystallographic textures obtained in the present study from uniaxial compression tests can be qualitatively interpreted in terms of the texture evolution known from rolling. The reason for that is the dominance of the compressive stress component for the texture evolution in either case. Plane strain states such as used for the idealization of rolling processes (neglecting the complex forward and backward shear processes in the actual rolling gap) can be approximated by the Tucker stress state. This loading situation is characterized by a compressive stress component in the sheet normal direction and a tensile stress in the forward (rolling) direction. This means that, except for the longitudinal stress component, rolling and compressive deformation states are comparable. The strong similarity between the two types of textures was also experimentally observed in detailed texture studies on steels that were conducted on uniaxial large-scale compressive tests using a 2.5 MN hot press [9,25,26].

### 3.4. Stress–strain curves

Fig. 7a shows the stress–strain curves of specimen 1 (alloy 0.5CMnSiCr) and specimens 2 and 3 (alloy 0.5C)

taken during superplastic deformation at 973 K. The flow stress reveals a downward trend (specimen 1, from 125 MPa to 113 MPa; specimen 2, from 122 MPa to 110 MPa; specimen 3, from 107 MPa to 94 MPa) with increasing strain within  $R_t$ . For the plain alloy 0.5C, the flow stress of specimen 2 containing 75 vol.% pearlite is  $\sim 15$  MPa higher than that of specimen 3 containing 93 vol.% martensite during warm deformation. The flow stress of the Mn–Si–Cr alloyed specimen 1, containing 100 vol.% martensite, is similar to that of specimen 3 within regimes  $R_{11}$ – $R_{12}$  and  $R_{21}$ – $R_{22}$  (i.e.  $R_{11}$ ,  $R_{12}$ ,  $R_{21}$  and  $R_{22}$ ), while the former is higher than the latter within regimes  $R_{13}$ – $R_{15}$  and  $R_{23}$ – $R_{25}$ . The  $m$ -value within strain regimes  $R_1$  and  $R_2$  at 973 K is shown in Table 2. It can be seen that specimen 1 (alloy 0.5CMnSiCr) exhibits superplastic characteristics ( $m > 0.3$ ) within  $R_{21}$ – $R_{24}$  (i.e. at a strain rate of  $10^{-4}$ – $10^{-3}$  s $^{-1}$ ). The  $m$ -value of specimens 2 and 3 (alloy 0.5C) is low ( $m < 0.23$ ) within the regimes  $R_1$  and  $R_2$ .

Fig. 7b exemplarily shows the full stress–strain curves for the WQ large-scale tensile samples of the alloy 1.3CMnSiCr at 973 K and 1073 K, respectively. Fig. 7c presents the stress–strain curves of different small-scale samples of alloy 1.3CMnSiCr during superplastic deformation at different temperatures. The deformation steps, sequence and conditions are the same as for the procedure outlined in Fig. 7a.

### 3.5. Elongation

The AC and WQ tensile samples of alloys 0.5CMnSiCr and 1.3CMnSiCr were obtained from the center of the rolled plates after large-scale thermomechanical treatment (1 h holding at 1223 K plus 50% reduction at

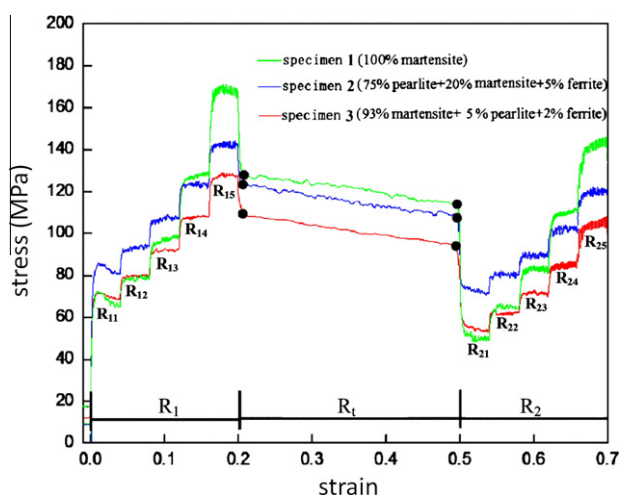


Fig. 7a. Stress–strain curves obtained for specimen 1 (alloy 0.5CMnSiCr) and specimens 2, 3 (alloy 0.5C) during superplastic warm deformation at 973 K. The superplastic deformation conditions are given in Table 1. All superplastic deformation cycles consist of three sequential strain regimes, namely, the first strain regime ( $R_1$ ), the transition regime ( $R_t$ ) and the second strain regime ( $R_2$ ). regimes  $R_1$  ( $R_2$ ) with a total true strain of 0.2 consist of five sequential parts, i.e.  $R_{11}$ ,  $R_{12}$ ,  $R_{13}$ ,  $R_{14}$  and  $R_{15}$  (similarly,  $R_{21}$ ,  $R_{22}$ ,  $R_{23}$ ,  $R_{24}$  and  $R_{25}$ ). Each of these sub-regimes imposed a true strain step of 0.04 at a specific strain rate specified in Table 1 (e.g.  $R_{11}$  represents a true strain of 0.04 at  $10^{-4} \text{ s}^{-1}$  within the strain regime  $R_1$ ). A true strain of 0.3 at  $10^{-3} \text{ s}^{-1}$  was applied within  $R_t$  in order to focus on the difference in strain rate sensitivity between deformation regimes  $R_1$  and  $R_2$ . The line colors indicate the differences in the starting microstructures (specimens 1–3) obtained after the pre-processing steps before superplastic forming according to Figs. 1 and 3. Specimen 1 (alloy 0.5CMnSiCr) contained 100 vol.% martensite before superplastic forming. Specimen 2 (alloy 0.5C) contained pearlite (~75 vol.%), martensite (~20 vol.%), and ferrite (~5 vol.%) before superplastic forming. Specimen 3 (alloy 0.5C) contained martensite (~93 vol.%), pearlite (~5 vol.%), and ferrite (~2 vol.%) before superplastic forming.

1223–1073 K followed by cooling). Previous studies [14,18] showed that the optimum superplastic temperature range for these steels is around the  $A_1$  temperature (usually slightly below  $A_1$ ). Therefore, 973 K and 1023 K (just below  $A_1$ ) were chosen as the tensile testing temperatures. Figs. 8 and 9 show the results at 973 K and 1023 K, respectively. For alloy 1.3CMnSiCr, the average elongation of the WQ samples (432% at 973 K and 530% at 1023 K; Fig. 7b) is higher than that observed for the AC samples (257% at 973 K and 233% at 1023 K). For the 0.5CMnSiCr alloy, the average elongation of the WQ samples (217%) is close to that determined for the AC samples at 973 K (218%), while the elongation of the former (205%) is slightly lower than that of the latter (340%) at 1023 K.

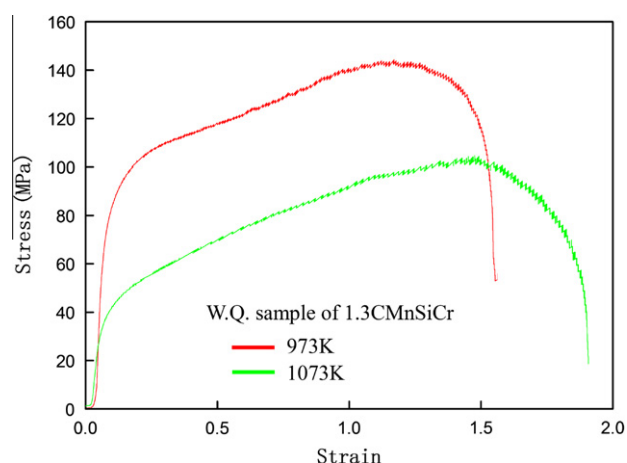


Fig. 7b. Exemplary full stress–strain curves for the WQ tensile samples of the alloy 1.3CMnSiCr at 973 K and 1073 K, respectively.

The WQ samples of 1.3CMnSiCr exhibit excellent superplasticity (elongation ~600% at 1023 K). The tensile test results obtained for the AC and WQ samples (note the short gauge length) of 1.3CMnSiCr at 1023 K are shown in Fig. 10. The quantification of the elongation for such a limited central gauge length (5 mm, owing to the small zone of homogeneous temperature) reveals a drastic increase in elongation of the WQ samples from 600% to 900%.

The WQ cylinders (6 × 10 mm) that were cut from the rolled plates after large-scale thermomechanical treatment had a hardness of about HRC 63–64 (hardness according to the Rockwell scale). After superplastic forming at 973 K the final material had a much lower hardness of HRC 32–33, owing to its homogeneous ferrite–carbide matrix.

#### 4. Discussion

##### 4.1. Microstructures obtained after small specimen thermomechanical processing

The  $A_{e3}$  temperatures of alloys 0.5CMnSiCr and 0.5C are <1073 K, i.e. austenite does not transform during pre-deformation at 1073 K (Fig. 1a and b). A previous study [27] showed that Mn alloying retards pearlite transformation during cooling. In the current alloy concept, Mn–Si–Cr alloying improves the hardenability of alloy 0.5CMnSiCr. As a result, the austenite in alloy 0.5CMnSiCr transforms fully into martensite during AC after

Table 2  
 $m$ -Value within the first and second strain regimes during superplastic warm deformation at 973 K.

Strain regime	First strain regime ( $R_1$ )				Second strain regime ( $R_2$ )			
	$R_{11}$ – $R_{12}$	$R_{12}$ – $R_{13}$	$R_{13}$ – $R_{14}$	$R_{14}$ – $R_{15}$	$R_{21}$ – $R_{22}$	$R_{22}$ – $R_{23}$	$R_{23}$ – $R_{24}$	$R_{24}$ – $R_{25}$
$m$ of specimen 1	0.24	0.30	0.29	0.25	0.38	0.35	0.31	0.24
$m$ of specimen 2	0.16	0.20	0.15	0.12	0.13	0.15	0.15	0.13
$m$ of specimen 3	0.19	0.22	0.16	0.15	0.22	0.19	0.19	0.21

Specimen 1 (alloy 0.5CMnSiCr) and specimens 2–3 (alloy 0.5C) are obtained after the corresponding thermomechanical pre-processing steps in Fig. 1.

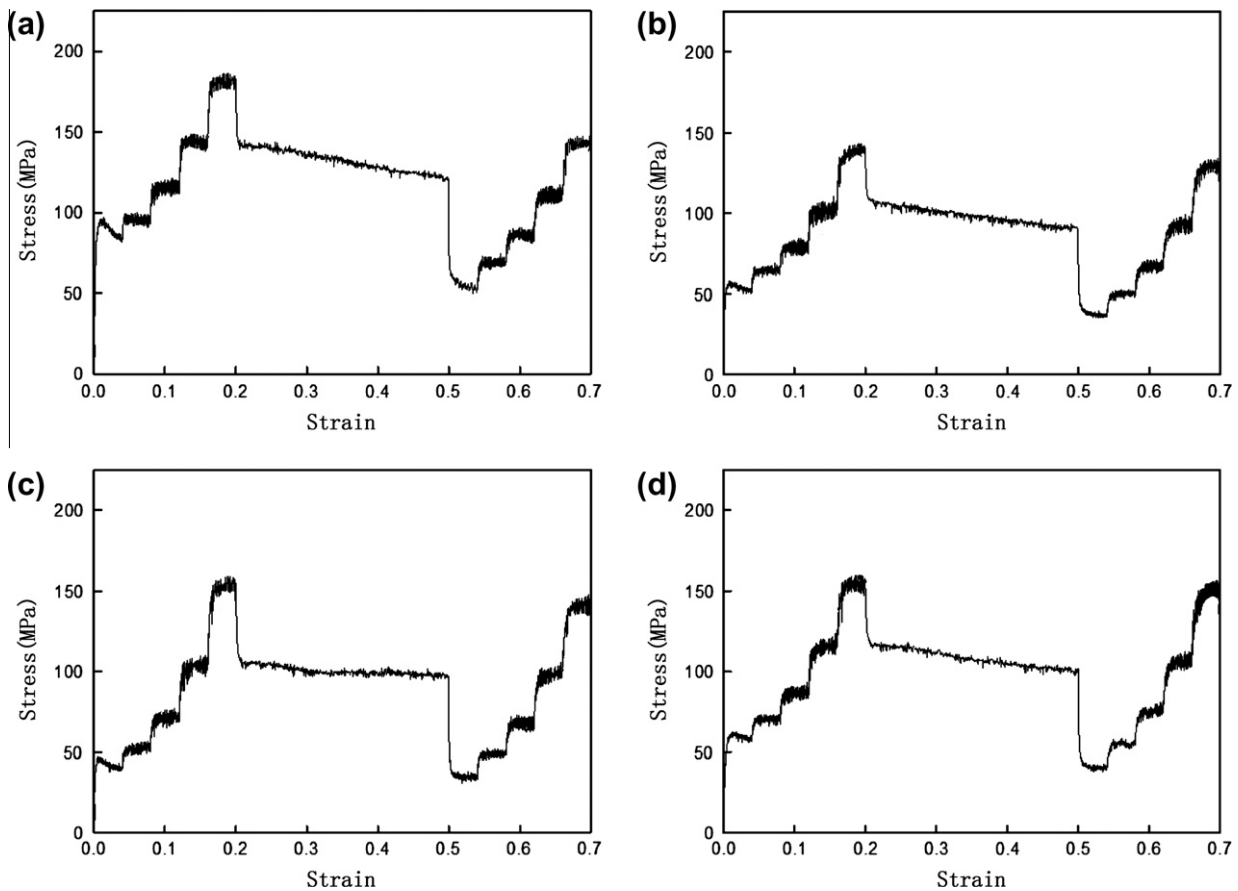


Fig. 7c. Stress–strain curves of different small-scale cylinders obtained for alloy 1.3CMnSiCr during superplastic warm deformation at different temperatures. The deformation steps, sequence and conditions are the same as for the procedure outlined in (a). (a) AC cylinder (973 K); (b) AC cylinder (1023 K); (c) WQ cylinder (973 K); (d) WQ cylinder (1023 K).

deformation. In contrast, most of the austenite in alloy 0.5C transforms to pearlite ( $\sim 75$  vol.% in specimen 2) during AC after pre-deformation. Even during water quenching after the thermomechanical deformation, some of the austenite in alloy 0.5C transforms to ferrite and pearlite ( $\sim 7$  vol.% in specimen 3). This indicates that the hardenability of alloy 0.5CMnSiCr is much better than that of alloy 0.5C. The hardenability is determined by the phase transformation (from austenite to martensite/ferrite/pearlite) during cooling after the preceding thermomechanical deformation above the  $A_{e3}$  temperature.

#### 4.2. Microstructure evolution during superplastic warm deformation

Fig. 3 shows the microstructures of specimen 1 (alloy 0.5CMnSiCr) and specimens 2 and 3 (alloy 0.5C) that evolve during superplastic deformation at 973 K. Pearlite lamellae break up and carbides spheroidize within the initial pearlite zone (solid circle, Fig. 3b). At the same time, DRX of ferrite occurs within the initial martensite zone (solid rectangle, Fig. 3b) because the critical strain required for DRX of ferrite during warm deformation is much smaller for lath martensite than for ferrite and pearlite [28].

Since specimens 1 and 3 contain a much larger martensite fraction than specimen 2, the DRX of ferrite revealed in Fig. 3f and d is more complete than that in Fig. 3b.

It was addressed in Ref. [28] that tempering of lath martensite for 300 s at 923 K led to the formation of carbides ( $\sim 0.1$   $\mu\text{m}$  in diameter) at grain boundaries. Therefore, it is conceivable that the precipitation of carbides is finished within the martensite zone soon after the onset of warm deformation at 973 K. Moreover, carbon diffusion is accelerated during warm deformation, promoting the precipitation of carbides [29]. With increasing strain, the average size of the carbides at grain boundaries increases, and the density of carbides inside the grains drops [30]. The resulting carbide dispersion is controlled by Ostwald ripening. In Fig. 3f, submicron-sized carbides ( $\sim 0.5$   $\mu\text{m}$ ) are located at ferrite grain boundaries, and only a small density of nanometer-sized carbides occurs inside the ferrite grains. The submicron-sized carbides precipitate at hetero-phase interfaces and martensite blocks soon after the onset of superplastic forming. Owing to the contribution of interface diffusion, they can grow fast at the expense of nanometer-sized carbides precipitating inside the martensite blocks. This is revealed in Fig. 3d, where nanometer-sized carbides are dispersed inhomogeneously. The zones lacking

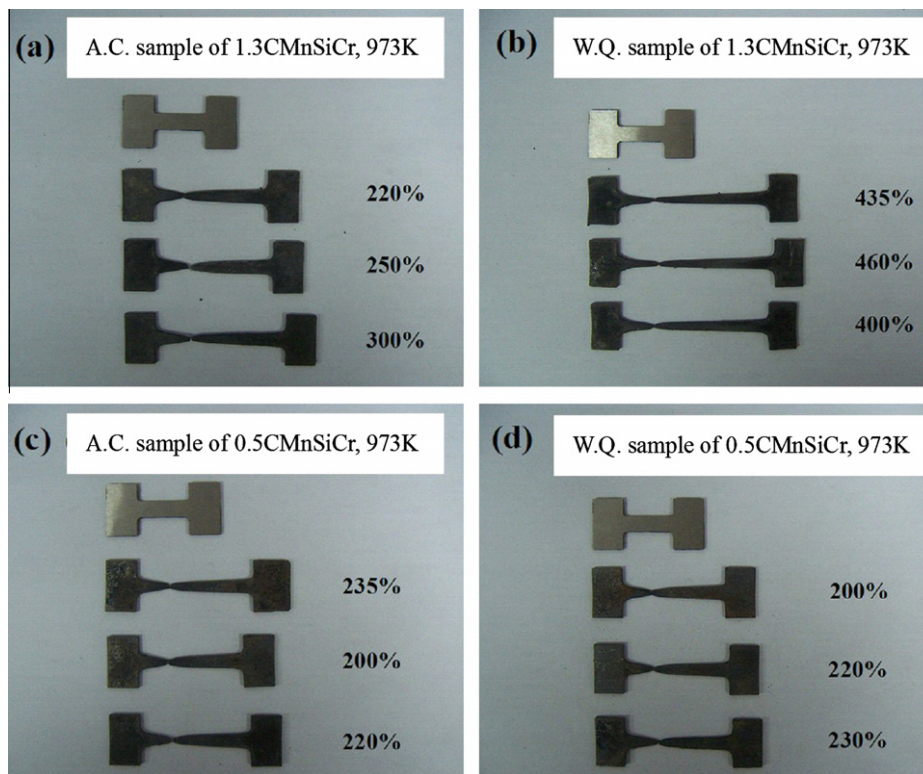


Fig. 8. Tensile test results obtained from superplastic forming at 973 K: (a) AC samples and (b) WQ samples of alloy 1.3CMnSiCr; (c) AC samples and (d) WQ samples of alloy 0.5CMnSiCr.

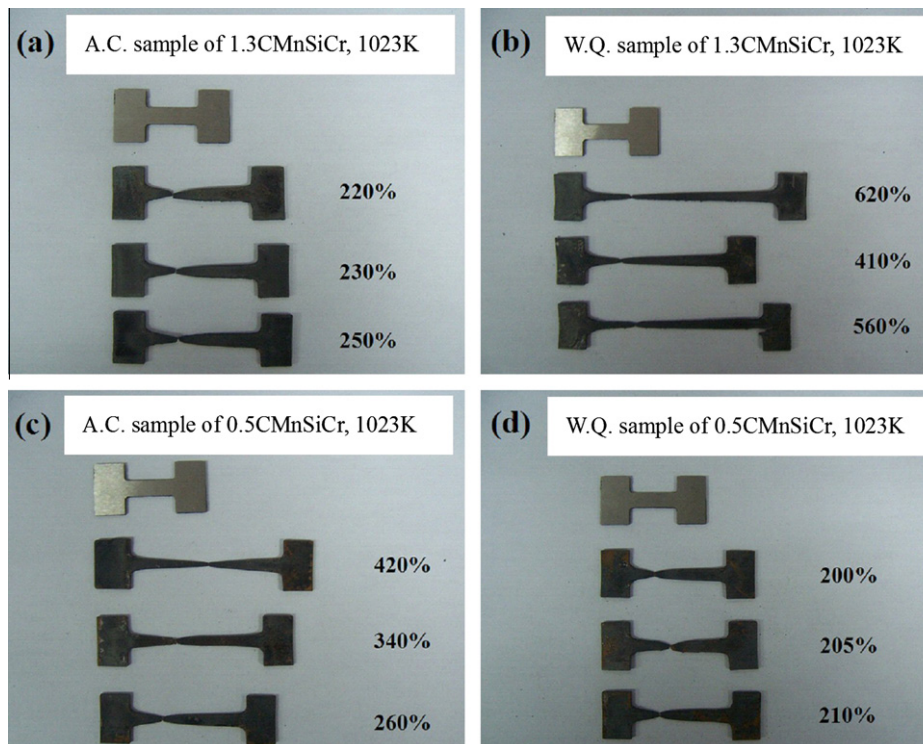


Fig. 9. Tensile test results obtained from superplastic forming at 1023 K: (a) AC samples and (b) WQ samples of alloy 1.3CMnSiCr; (c) AC samples and (d) WQ samples of alloy 0.5CMnSiCr.

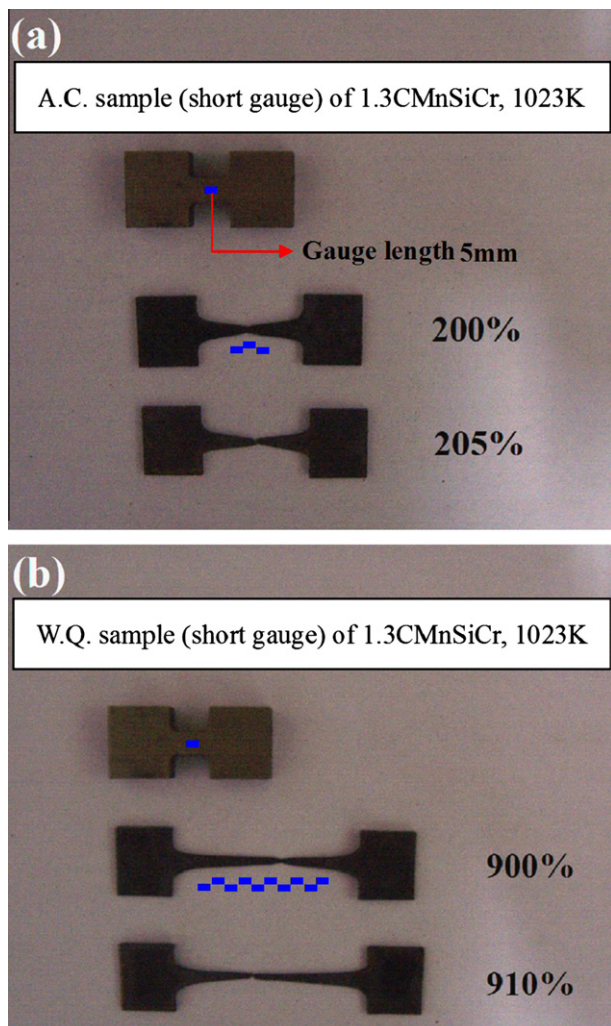


Fig. 10. Tensile test results obtained for (a) AC samples and (b) WQ samples (short gauge length: 5 mm) of alloy 1.3CMnSiCr at 1023 K.

the nanometer-sized carbides are formed through the dissolution of nanometer-sized carbides inside the martensite blocks. However, a large amount of these carbides still distributes inside the ferrite grains, as revealed in Fig. 3d. These observations suggest that there is a specific precipitation mechanism that is responsible for the formation of these small carbides. Ferrite recovery includes mechanisms such as dislocation accumulation, formation of low-angle grain boundaries and polygonization. During superplastic deformation, dislocations are multiplied and accumulated. A previous study [31] showed that the bonding energy between the carbon atoms and dislocations in ferrite is larger than that between the carbon and iron atoms in cementite. Therefore, nanometer-sized carbides precipitating inside martensite blocks dissolve, and the released carbon atoms diffuse, probably via dislocation cores, to form Cottrell atmospheres [31,32]. With increasing strain, low-angle grain boundaries are formed through dislocation reorganization and annihilation. At the same time, the solubility of carbon atoms in ferrite drops with the decrease in dislocation density, which results in the re-precipitation of

nanometer-sized carbides. Consequently, the dispersed nanometer-sized carbides revealed in Fig. 3d are assumed to be formed mostly in terms of a dissolution and re-precipitation mechanism [33,34]. In addition, the average size of submicron-sized carbides in Fig. 3d ( $\sim 0.8 \mu\text{m}$ ) is larger than that in Fig. 3f ( $\sim 0.5 \mu\text{m}$ ). This is caused by the effect of Mn–Si–Cr alloying and will be discussed below.

Previous studies [35,36] showed that ferrite nuclei formed by DRX were located near large carbides ( $>0.5 \mu\text{m}$ ), owing to the strain gradient that exists in the vicinity of these precipitates. Therefore, DRX of ferrite most probably occurs near those submicron-sized carbides during superplastic warm deformation. At the same time, ferrite recovery [37] is promoted with increasing strain.

#### 4.3. Effects of Mn, Si and Cr on microstructure evolution during superplastic deformation

The density of submicron-sized carbides in Fig. 3f is larger than that in Fig. 3d. This is attributed to the effect of Si which suppresses carbide precipitation [38,39]. For specimen 1 (Mn–Si–Cr alloyed), the interfaces of the martensite laths are not the preferential precipitation sites of carbides due to the influence of Si. The preferential precipitation sites are rather located at hetero-phase interfaces and martensite blocks soon after the onset of superplastic deformation. Owing to the contribution of interface diffusion, the carbides precipitating at the hetero-phase interfaces and martensite blocks grow fast, at the expense of the carbides at the martensite laths, and finally lead to the formation of a high density of submicron-sized carbides, as shown in Fig. 3f. For specimen 3 (no Mn–Si–Cr alloying), the interfaces of martensite laths also act as favorable sites for precipitation of carbides. Since each martensite block contains multiple laths, the precipitation at martensite laths competes with that at hetero-phase interfaces and martensite blocks so that the frequency of precipitation events at hetero-phase interfaces and martensite blocks is reduced. Fig. 11 schematically shows the carbide precipitation behavior of specimen 1 (alloy 0.5CMnSiCr) and specimen 3 (alloy 0.5C) soon after the onset of superplastic warm deformation. Owing to the effect of Si, the density of precipitation sites at hetero-phase interfaces and martensite blocks is higher than that at martensite laths in specimen 1 (alloy 0.5CMnSiCr). Without the presence of Si, the density of the precipitation sites at martensite laths is close to that at hetero-phase interfaces and martensite blocks in specimen 3 (alloy 0.5C). The difference in precipitation behavior between the two samples leads to the effect that a higher density of submicron-sized carbides exists in the microstructure revealed in Fig. 3f compared with that shown in Fig. 3d. The precipitation discussed here occurs soon after the onset of superplastic deformation, which should be distinguished from the re-precipitation of nanometer-sized carbides known from the dissolution and re-precipitation mechanism. However, the slow diffusion of Mn, Si and Cr retards the growth of the carbides precipitating at hetero-phase interfaces and martensite blocks. Conse-

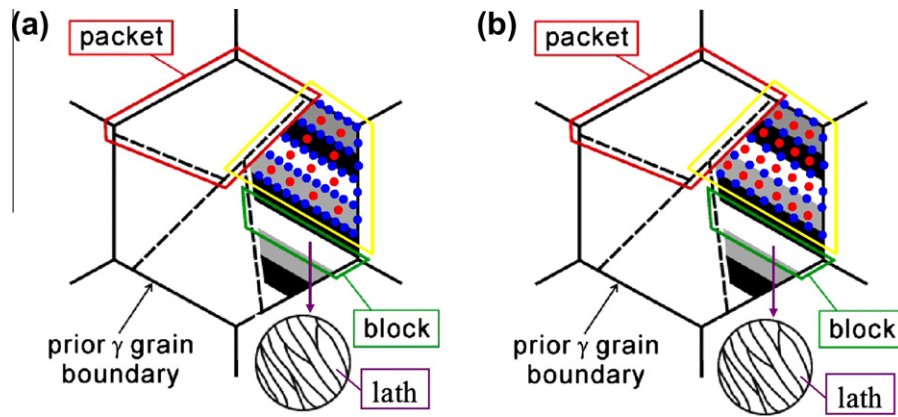


Fig. 11. Carbide precipitation behavior of (a) specimen 1 (alloy 0.5CMnSiCr) and (b) specimen 3 (alloy 0.5C) soon after the onset of warm deformation at 973 K (blue dots, the precipitation sites at hetero-phase interfaces and martensite blocks; red dots, the precipitation sites at martensite laths).

quently, the submicron-sized carbides revealed in Fig. 3f are smaller than those in Fig. 3d. In addition, specimen 1 has a higher density of precipitation sites at hetero-phase interfaces and martensite blocks compared with specimen 3. Therefore, the total carbon content is blended into more submicron-sized carbides, and the average size of the submicron-sized carbides is limited during superplastic forming of specimen 1.

DRX of ferrite mainly occurs near the submicron-sized carbides during warm deformation. Therefore, more ferrite nuclei are obtained by DRX due to a higher density of submicron-sized carbides in specimen 1 (compared with specimen 3). The carbides act as obstacles for the growth of ferrite grains due to Zener pinning. As a result, the ferrite grains revealed in Fig. 6a are much finer than those presented in Fig. 6d. In addition, Cr stabilizes the carbides [17] so that the fine precipitates at the ferrite grain boundaries prevents ferrite grain coarsening during superplastic forming.

#### 4.4. Role of carbon during superplastic deformation

According to the Lifshitz–Slyozov–Wagner (LSW) theory [30,40], the kinetic equation for spherical carbide coarsening is given, when carbon diffusion controls the process, by

$$\bar{r}^3 - \bar{r}_0^3 = \frac{8\gamma V_0^2 x_c D_c}{9RT} \cdot (t - t_0) \quad (1)$$

In this equation,  $r$  is the average radius of the carbides at time  $t$ ,  $r_0$  is their initial radius at the onset of coarsening,  $\gamma$  is the carbide–ferrite interface energy,  $D_c$  is the diffusion coefficient of carbon,  $x_c$  is the solubility of carbon in ferrite,  $R$  is the gas constant,  $T$  is the absolute temperature, and  $V_0$  is the molar volume of the carbides. Fig. 3f shows that the average size of the carbides is  $\sim 0.5 \mu\text{m}$  in diameter after superplastic forming of specimen 1 (alloy 0.5CMnSiCr). Then  $D_c$  can be calculated as  $2.55 \times 10^{-3} \text{ cm}^2 \text{ s}^{-1}$  according to Eq. (1) (using  $\gamma = 0.7 \text{ J m}^{-1}$  [41],  $V_0 = 2.397 \times 10^{-5} \text{ m}^3 \text{ mol}^{-1}$  [42],  $x_c = 7.7 \times 10^{-4}$  [43]).

Here, the diffusion of carbon occurs during superplastic deformation at 973 K. Grain boundary diffusion or even pipe diffusion along dislocations is assumed to be the dominant diffusion mechanism due to the high density of grain boundaries and dislocations in the material. Therefore,  $D_c$  is considered the grain boundary diffusion coefficient and calculated as  $4.4 \times 10^{-5} \text{ cm}^2 \text{ s}^{-1}$  according to Eq. (2) [44,45].

$$D_c = 6.2 \times 10^{-3} \times \exp\left(-\frac{40,000(\text{J/mol})}{RT}\right) (\text{cm}^2/\text{s}) \quad (623\text{--}1123 \text{ K}) \quad (2)$$

The difference in the two calculated diffusion coefficients of carbon indicates that Mn–Si–Cr alloying accelerates the diffusion of carbon, promoting carbide coarsening during superplastic warm deformation of the initial martensitic microstructure. The average size of submicron-sized carbides revealed in Fig. 3d ( $\sim 0.8 \mu\text{m}$ ) is larger than that presented in Fig. 3f ( $\sim 0.5 \mu\text{m}$ ), which suggests that the coarsening of carbides should be faster even without Mn–Si–Cr alloying. Therefore, it is supposed that the coarsening of carbides is controlled by the slow diffusion of Mn, Si and Cr. Although Mn–Si–Cr alloying retards the coarsening of the carbides, a large density of submicron-sized carbides was formed at a low strain (i.e. true strain 0.7) during warm deformation at 973 K. This is attributed to the large amount of carbide precipitation sites at the hetero-phase interfaces and martensite blocks. Furthermore, the additional contribution of grain boundary diffusion (or pipe diffusion) contributes to the formation of submicron-sized carbides.

#### 4.5. Factors affecting the superplasticity of Mn–Si–Cr–C steels

##### 4.5.1. Thermomechanical processing prior to superplastic forming

After initial thermomechanical processing (Fig. 1b), specimen 2 with 75 vol.% pearlite and specimen 3 with

93 vol.% martensite were obtained (both alloy 0.5C). The difference in microstructure between the two is due to the different cooling rates. At 973 K, the flow stress of specimen 2 is  $\sim 15$  MPa above that of specimen 3. This indicates that the thermomechanical processing affects the subsequent superplastic forming owing to its influence on the starting microstructures. Table 2 shows that the  $m$ -value for specimen 2 is lower than that for specimen 3 within regime  $R_2$  (see details in Fig. 7a) during superplastic forming at 973 K. The difference in  $m$ -value between the two specimens 2 and 3 indicates a basic influence of the preceding thermomechanical processing on the subsequent superplastic flow behavior. However, the AC and WQ tensile samples of alloy 1.3CMnSiCr obtained after large-scale thermomechanical treatment (1 h holding at 1223 K plus 50% reduction at 1223–1073 K followed by cooling) exhibit different elongations at 973 K (Fig. 8a and b). This difference is caused by the differences in microstructure between the AC and WQ samples (Fig. 4a and b).

#### 4.5.2. Effect of Mn–Si–Cr alloying on the formation of superplastic microstructures

It is observed that the range of alloying studied here, (2–2.5)Mn–(1.5–2)Si–(0.8–1.5)Cr, not only improves hardenability, but also facilitates the formation of microstructures that promote structural superplasticity. More specifically, a homogeneous ferrite plus spherical carbide duplex microstructure is obtained during superplastic forming. The high hardenability of Mn–Si–Cr–C steels is beneficial for obtaining relatively fine martensite (martensite blocks  $< 10 \mu\text{m}$ ) after a thermomechanical process which consists of austenitization plus true strain of 1.2, followed by fast cooling. During subsequent superplastic forming of the initial martensite microstructure, the high interface density provides multiple carbide precipitation sites and leads to a homogeneous precipitation topology. Furthermore, Mn–Si–Cr alloying seems to increase the density of carbide precipitation sites at hetero-phase interfaces and martensite blocks, thereby resulting in a high density of submicron-sized carbides. These carbides grow at the expense of the carbides precipitating at martensite laths. The ferrite is essentially formed by DRX. Consequently, the material assumes a fine ferrite grain size  $\sim 1.5 \mu\text{m}$  at low superplastic strains (i.e. true strain of 0.7) at 973 K. The submicron-sized spherical carbides located at the ferrite grain boundaries act as obstacles for the growth of ferrite grains due to Zener pinning during superplastic forming [13]. As mentioned above, the microstructure of alloy 0.5CMnSiCr (Fig. 3f) is much finer and more homogeneous than that of alloy 0.5C in Fig. 3d after warm deformation at 973 K. The pole figures (Fig. 6g) indicate that intense subgrain formation, and probably also subgrain rotation, occurs during ferrite recovery in the course of warm deformation of alloy 0.5CMnSiCr. These two phenomena also contribute to a gradual deformation-driven grain refinement and, thereby, might promote grain boundary sliding during superplastic deformation [19].

#### 4.5.3. Effect of carbon content on microstructure and superplasticity

A previous study [28] showed that the martensite block size decreased with an increase in carbon content. It was also observed that martensite refinement promoted ferrite recrystallization during the subsequent superplastic deformation. This means that an increase in the carbon content is advantageous for realizing superplasticity in the current alloys. Also, the amount and dispersion of carbides suppressing ferrite coarsening is increased with higher carbon content, which further promotes superplasticity. In the present work, the elongation of the WQ samples of alloy 1.3CMnSiCr is higher than that of the WQ samples of alloy 0.5CMnSiCr at 973 K and 1023 K (Figs. 8 and 9). However, the elongation of AC samples of alloy 1.3CMnSiCr is similar to or even lower than that of AC samples of alloy 0.5CMnSiCr at 973 K and 1023 K. This contradiction is due to the difference in the microstructure of the AC samples prior to superplastic tensile testing. The AC microstructure of alloy 1.3CMnSiCr contains mainly lamellar pearlite, while the AC microstructure of alloy 0.5CMnSiCr is composed mostly of martensite. The present results showed, however, that martensite transforms to a duplex microstructure consisting of ferrite and spherical carbides soon after the onset of superplastic warm deformation at 973 K. Therefore, the AC samples of 0.5CMnSiCr show higher elongations than those of 1.3CMnSiCr.

#### 4.6. Elongations and $m$ -values of Mn–Si–Cr–C steels

A previous study [46] showed that the final  $m$ -value determines the elongation to fracture. The  $m$ -value within the regimes  $R_{21}$ – $R_{22}$  is higher than that within  $R_{11}$ – $R_{12}$  (details in Fig. 7a) during superplastic deformation of specimen 1 (alloy 0.5CMnSiCr) at 973 K (Table 2). In Fig. 8c and d, the elongation of alloy 0.5CMnSiCr (with a microstructure similar to that of specimen 1, i.e. martensite) reaches a value of 200% at 973 K. Nevertheless, as discussed above, a high  $m$ -value alone is not sufficient to obtain a high elongation, especially when microstructures contain brittle phases (e.g. martensite and carbides). The occurrence of brittle phases may result in a low elongation even at a high  $m$ -value. Therefore, special attention is placed on the relationship between the  $m$ -value and the resulting elongation of Mn–Si–Cr–C steels. Table 3 shows the  $m$ -value of alloy 1.3CMnSiCr within the superplastic

Table 3  
 $m$ -Value of alloy 1.3CMnSiCr within the second strain regime during superplastic warm deformation.

Second strain regime ( $R_2$ )	$R_{21}$ – $R_{22}$	$R_{22}$ – $R_{23}$	$R_{23}$ – $R_{24}$	$R_{24}$ – $R_{25}$
$m$ of AC cylinder at 973 K	0.38	0.32	0.28	0.23
$m$ of AC cylinder at 1023 K	0.43	0.44	0.35	0.30
$m$ of WQ cylinder at 973 K	0.49	0.47	0.41	0.32
$m$ of WQ cylinder at 1023 K	0.46	0.47	0.36	0.31

The AC and WQ cylinders are obtained from the center of the AC and WQ plates (30 mm) after rolling, respectively.

strain regime  $R_2$ . The AC and WQ cylinders used for the measurement of the  $m$ -value are 6 mm in diameter and 10 mm in length. They were cut from the center of the rolled plates after large-scale thermomechanical treatment (1 h holding at 1223 K plus 50% reduction at 1223–1073 K followed by cooling). The measurement of the corresponding  $m$ -values is conducted through superplastic warm deformation with the same deformation conditions as used for specimens 1–3, as shown in Table 1. Fig. 7c shows the corresponding stress–strain curves of the different small-scale cylinders of alloy 1.3MnSiCr (AC and WQ; 973 K and 1073 K) during superplastic warm deformation at different temperatures. The deformation steps, sequence and conditions are the same as for the procedure outlined in Fig. 7a.

The microstructures of the cylinders are the same as those of the samples used for tensile testing, owing to identical sampling positions. Since the strain rate is kept at  $\sim 10^{-4} \text{ s}^{-1}$  during tensile testing, the average  $m$ -value within regimes  $R_{21}$ – $R_{23}$  (i.e. at  $10^{-4}$ – $4 \times 10^{-4} \text{ s}^{-1}$ , Fig. 7a) is used during superplastic deformation to achieve similar testing conditions. The average  $m$ -value of the AC cylinders is  $\sim 0.35$  at 973 K and  $\sim 0.44$  at 1023 K (the average elongation of AC samples is  $\sim 257\%$  at 973 K and  $\sim 233\%$  at 1023 K). The average  $m$ -value of the WQ cylinders is  $\sim 0.48$  at 973 K and  $\sim 0.47$  at 1023 K (the average elongation of WQ samples is  $\sim 432\%$  at 973 K and  $\sim 530\%$  at 1023 K). As a rule, the WQ cylinders exhibit higher  $m$ -values, and this leads to higher elongations in comparison with the AC samples. However, it was also observed that higher  $m$ -values alone do not necessarily lead to higher elongations. For example, the average  $m$ -value of the AC cylinders at 1023 K ( $\sim 0.44$ ) is higher than that of the AC cylinders ( $\sim 0.35$ ) at 973 K. In contrast, the average elongation at 1023 K ( $\sim 233\%$ ) is lower than that at 973 K ( $\sim 257\%$ ). This indicates that a higher  $m$ -value is necessary, but not sufficient, for obtaining higher superplastic elongations in Mn–Si–Cr–C steels. In future, with regard to the further development of Mn–Si–Cr–C steels with excellent superplasticity, the measurement of the  $m$ -value can be applied to predict superplasticity in advance and should then be combined with tensile testing to identify the optimal superplastic deformation regime. It must also be considered that the specific tensile testing conditions affect the elongation results. A limited gauge area of uniform temperature may lead to non-uniform conditions and smaller elongations during testing.

## 5. Conclusions

- (1) As an effective way of improving hardenability, (2–2.5)Mn–(1.5–2)Si–(0.8–1.5)Cr alloying is beneficial for obtaining martensite through a thermomechanical process (austenitization plus true strain of 1.2 followed by fast cooling) in steels. The strain rate sensitivity of (1.2–1.5)C–(2–2.5)Mn–(1.5–2)Si–(0.8–1.5)Cr steels consisting initially of martensite and spherical carbides (before superplastic forming) reaches values up to nearly 0.5 and a maximum superplastic elongation of as much as 900% at 1023 K. Such a high elongation is achieved for the first time in the field of low-alloyed steels produced through conventional processing.
- (2) Mn–Si–Cr alloying seems to increase the density of carbide precipitation sites at hetero-phase interfaces and martensite blocks soon after the onset of superplastic forming at 973–1023 K (below austenite–pearlite transformation). Owing to the contribution of interface diffusion, the carbides precipitating at hetero-phase interfaces and martensite blocks grow fast at the expense of the carbides precipitating at martensite laths. Simultaneously, DRX and recovery of ferrite occur, finally leading to the formation of a fine and homogeneous duplex microstructure (ferrite plus spherical carbides) with a ferrite grain size  $\sim 1.5 \mu\text{m}$  in Mn–Si–Cr–C steels. The spherical carbides include submicron-sized carbides at the ferrite grain boundaries and nanometer-sized carbides inside the ferrite grains. Nanometer-sized carbides are formed via dissolution and re-precipitation.
- (3) Redistribution of Mn, Si and Cr occurs between the ferrite and carbides during superplastic forming at 973–1023 K. Carbide coarsening is controlled by the slow diffusion of Mn, Si and Cr. Although Mn–Si–Cr alloying may accelerate carbon diffusion, carbide coarsening is suppressed owing to the slow diffusion of Mn, Si and Cr. As a result, the average size of submicron-sized carbides at the ferrite grain boundaries is reduced.
- (4) Subgrain formation occurs during ferrite recovery in the course of superplastic forming of Mn–Si–Cr–C steels at 973 K. This could promote grain boundary sliding and, hence, superplasticity.
- (5) Thermomechanical processing before superplastic forming, Mn–Si–Cr alloying, carbon content and superplastic deformation conditions (temperature, strain rate) are the main factors affecting superplastic flow, properties, and microstructures of low-alloyed Mn–Si–Cr–C steels.

## Acknowledgements

Electron microscopy analysis was supported by Beijing National Center for Electron Microscopy, Department of Materials Science and Engineering, Tsinghua University.

## References

- [1] Jong MD, Rathenau GW. Acta Metall 1959;7:246.
- [2] Takei H, Nakasa K. J Jpn Inst Met 1971;35:1063.
- [3] Oyama T, Sherby OD, Wadsworth J, Walser B. Scripta Metall 1984;18:799.
- [4] Sherby OD, Oyama T, Kum DW, Walser B, Wadsworth J. J Met 1985;37:50.
- [5] Tsuzaki K, Sato E, Furimoto S, Furuhashi T, Maki T. Scripta Mater 1999;40:675.

- [6] Shin DH, Park KT, Kim YS. *Scripta Mater* 2003;48:469.
- [7] Valiev RZ, Langdon TG. *Prog Mater Sci* 2006;51:881.
- [8] Zhilyaev AP, Langdon TG. *Prog Mater Sci* 2008;53:893.
- [9] Song R, Ponge D, Raabe D, Kaspar R. *Acta Mater* 2005;53:845.
- [10] Tsuji N, Ueki R, Minamino Y, Saito Y. *Scripta Mater* 2002;46:305.
- [11] Ohmori A, Torizuka S, Nagai K. *ISIJ Int* 2004;44:1063.
- [12] Okitsu Y, Takatab N, Tsuji N. *Scripta Mater* 2009;60:76.
- [13] Zhang H, Zhang L, Cheng X, Xu L, Bai B. *Scripta Mater* 2010;62:798.
- [14] Zhang H, Cheng X, Zhang L, Bai B. *Mater Sci Eng A* 2010;527:5430.
- [15] Orhan N, Kurt B. *J Mater Process Technol* 2003;136:174.
- [16] Sherby OD. *ISIJ Int* 1999;39:637.
- [17] Wadsworth J, Sherby OD. *J Mater Sci* 1978;13:2645.
- [18] Zhang H, Zhang L, Cheng X, Bai B. *Acta Mater* 2010;58:6173.
- [19] Nieh TG, Wadsworth J, Sherby OD. *Superplasticity in metals and ceramics*. New York: Cambridge University Press; 2005.
- [20] Woodford DA. *Trans ASM* 1969;62:291.
- [21] <http://www.mediacy.com>.
- [22] Syn CK, Lesuer DR, Sherby OD. *Metall Mater Trans A* 1994;25:1481.
- [23] Raabe D. *Steel Res* 1995;66:222.
- [24] Song R, Ponge D, Raabe D, Speer JG, Matlock DK. *Mater Sci Eng A* 2006;441:1.
- [25] Hölscher M, Raabe D, Lücke K. *Steel Res* 1991;62:567.
- [26] Storojeva L, Ponge D, Kaspar R, Raabe D. *Acta Mater* 2004;52:2209.
- [27] Yang L, Fang HS, Meng ZH. *Acta Metall Sin* 1992;28:16.
- [28] Poorganji B, Miyamoto G, Maki T, Furuhashi T. *Scripta Mater* 2008;59:279.
- [29] Chen W, Li LF, Sun ZQ, Zhang Y, Yang WY. *Acta Metall Sin* 2009;45:697.
- [30] Li LF, Xia CQ, Sun ZQ, Yang WY. *Acta Metall Sin* 2010;46:19.
- [31] Gavriljuk VG. *Scripta Mater* 2001;45:1469.
- [32] Wilde J, Cerezo A, Smith GDW. *Scripta Mater* 2000;43:39.
- [33] Languillaume J, Kapelski G, Baudalet B. *Acta Mater* 1997;45:1201.
- [34] Ivanisenko Y, Lojkowski W, Valiev RZ, Fecht HJ. *Acta Mater* 2003;51:5555.
- [35] Wang M, Li LF, Sun ZQ, Yang WY. *Acta Metall Sin* 2007;43:1009.
- [36] Calcagnotto M, Ponge D, Raabe D. *Mater Sci Eng A* 2010;527:2738.
- [37] Raabe D. *Scripta Metall* 1995;33:735.
- [38] Liu D, Bai B, Fang H, Zhang W, Gu J, Chang K. *Mater Sci Eng A* 2004;371:40.
- [39] Humphreys FJ, Hatherly M. *Recrystallization and related annealing phenomena*. 2nd ed. Amsterdam: Elsevier; 2004.
- [40] Devaux A, Nazé L, Molins R, Pineau A, Organista A, Guédou JY, et al. *Mater Sci Eng A* 2008;486:117.
- [41] Kramer JJ, Pound GM, Mehl RF. *Acta Metall* 1958;6:763.
- [42] Stuart H, Ridley N. *J Iron Steel Inst* 1966;204:711.
- [43] Swartz JC. *Trans Metall Soc AIME* 1969;245:1083.
- [44] Porter DA, Easterling KE. *Phase transformations in metals and alloys*. 2nd ed. Cheltenham: Nelson Thornes Ltd.; 1992.
- [45] Yong QL. *Secondary phases in steels*. Beijing: Metallurgical Industry Press; 2006.
- [46] Ghosh AK, Ayres RA. *Metall Trans A* 1976;7:1589.